Journal of Manufacturing Processes 32 (2018) 1–10

Microstructure and texture evolution of friction stir welded dissimilar aluminium alloys: AA2024 and AA6061

Mohammad Mahdi Moradi a, Hamed Jamshidi Aval a, Roohollah Jamaati a,∗,Sajjad Amirkhanlou b, Shouxun Ji b

a Department of Materials Engineering, Babol Noshirvani University of Technology, Shariati Ave., Babol 47148–71167, Iran

b Institute of Materials and Manufacturing, Brunel University London, Uxbridge UB8 3PH, United Kingdom

Keywords:

Aluminium alloys; Friction stir welding (FSW);Crystallographic texture; Electron backscattered diffraction (EBSD);Hardness

a b s t r a c t

In this study, the development of the microstructure and crystallographic texture during friction stir welding (FSW) of AA2024 and AA6061 dissimilar joint was investigated. Electron backscattered diffraction (EBSD) technique was employed to characterize the textures and revealed the evolution of microstructures during friction stir welding. Experimental results showed the grain refinement in the stirred zone through continuous and discontinuous recrystallization. The fraction of precipitates in the stirred zone of the retreating side was much higher than that of the advancing side. On the other hand, the extent of continuous dynamic recrystallization in the thermo mechanically affected zone (TMAZ) of the advancing side was lower than that of the retreating side and the recrystallized grains were rarely seen on the advancing side. The initial texture components of the sheets mainly consisted of {001}_100_ Cube and{011}_011_ Rotated Goss. The pole figures became asymmetric due to the inhomogeneous plastic deformation during FSW. The overall texture intensity was weaker on the advancing side and stronger on the retreating side than that in the starting materials. On the advancing side, {011}_211_ and {221}_012_texture components created and the _fibre (_111_//ND) shear texture developed on the retreating side. Correlation between the microstructure and texture proved that the discontinuous static recrystallization and/or meta-dynamic recrystallization occurred on the advancing side. Microhardness profile on the advancing side was almost identical, while the profile revealed three distinguishable regions on the retreating side.

1. Introduction

Joining of dissimilar wrought aluminium alloys especially heat treatable ones (2XXX, 6XXX, and 7XXX) is always a big challenge due to the differences in physical, mechanical, and chemical properties. Welding of dissimilar aluminium alloys is difficult via fusion processes since the intense heat generated by these techniques is responsible for the significant loss of strength in the joint because of thermally activated softening mechanisms [1–3]. Also, the fusion welding produces some defects such as cracks, voids, and inter-metallic compounds in the joints. [1–4]. Therefore, it is essential to decrease or eliminate these problems by employing joining technique in a solid or semi solid state. Friction stir welding (FSW) is an innovative solid-state joining process which transforms the metal into a plastic state at a temperature essentially below the melting point, and then mechanically stirs two metals together under high forging pressure to form a high-strength welded joint [1–4]. The yield and ultimate tensile strengths of the joints (joint efficiency) produced by FSW improve up to 100%, as reported in the literature [1–6], compared to the parent metal's strength. In the FSW, the materials that are being welded do not melt and solidify. For this reason, the aluminium alloys which are practically unweldable or difficult to be welded using fusion joining techniques are weldable with almost no defects by friction stir welding [1,4,7–9].Significant differences may be expected in terms of the microstructure and crystallographic texture on both the advancing and retreating sides of friction stir welded joints especially for dissimilar ones [1]. In general, the microstructure of FSW joints is divided into four regions: stirred zone (SZ), thermo mechanically affected zone (TMAZ), heat affected zone (HAZ), and base metal(BM).A number of researchers have investigated the microstructure and texture evolutions of similar and dissimilar heat treatable aluminium joints [4,10–13]. Xu et al. [10] reported the microstructure and texture evolutions of AA7005 aluminium alloy under FSW pro-cess. They demonstrated that the recrystallization occurred with the texture transformation and its corresponding activation of {111} slip, which indicates that the _111_//ND fibre textures con-tribute to the grain refinement in the stirred zone. Wang et al. [4] investigated the development of microstructure and texture during FSW in AA5052 and AA6061 dissimilar joint. They reported {001}_100_ Cube, {123}_634_ S components in the base metal gradually transform into {111}_112_ shear texture under stirring shear force. The high angle grain boundaries (HAGBs) distribution were the most significant in the stirred zone followed by the retreating side and then on the advancing side. Imam et al. [11] studied the microstructure and texture evolution during FSW of 6063 aluminium alloy. They found that the B/B texture component was dominated at the top of the weld joint, while the {111}_112_ components of A fibre and C component of B fibre were found at the bottom of the weld joint. Also for the similar crystallographic oriented grains nearby, the {111}_112_ components were observed on the retreating side, while this is replaced by the C component on the advancing side. Until now, a limited amount of in-depth study has been carried out for dissimilar heat treatable aluminium joints produced by FSW. Moreover, no attempt was found to investigate the microstructure and crystallographic texture of AA2024 and AA6061 dissimilar joint. Therefore, in the present paper, the microstructure and texture characteristics of the AA2024/AA6061 welded joints, such as

grain structure, grain misorientation distribution, the distribution of precipitation particles, and the texture components are studied by electron backscattered diffraction (EBSD).

2. Experimental procedure

The materials examined in this study were AA2024–T351 andAA6061–T6 with a dimension of 100 mm × 50 mm × 6 mm. One should note that the T351 is a temper in aerospace industry, which corresponds to solution treatment at about 500◦C followed by water quench, then stress relieves by stretching 1.5–3%, and finally ages at room temperature. The chemical composition of the alloys is listed in Table 1.The AA2024 and AA6061 sheets were adjusted on the advancing side and retreating side, respectively, on the machine bed with-out root gap. An AISI H13 hot work steel tool was used, having acronical geometry with 18 mm shoulder diameter, a 4◦conical cavity, a square frustum probe measuring 3.5–7 mm in diameter, and5.9 mm in length. The tool tilt was kept constant at 2◦for all experiments. The FSW was carried out with a rotational speed of 800 rpm and a welding speed of 31.5 mm/min. The welding direction (WD)was parallel to the rolling direction (RD) of both alloys. The trans-verse direction (TD) of the welded joint will be denoted as cross welding direction (CWD).Electron backscattered diffraction (EBSD) analysis was per-formed to investigate both the microstructure and texture at the mid-thickness of the samples as shown in Fig. 1. EBSD images were obtained using an FE-SEM (SUPRA 35VP, Carl-Zeiss Company, Jena, Germany) operated at a voltage of 20 kV, working distance of 12 mm, a tilt angle of 70◦and a step size of 0.5 _m. Specimens for EBSD characterization were mechanically ground and polished with standard metallurgical methods. The specimens subsequently electropolished with a solution of 30 pct. nitride acid and 70 pct. methanol at 12 V and −30◦C. Grain orientation map, grain boundary map, pole figure (PF), kernel average misorientation (KAM), and orientation distribution function (ODF) were obtained using EDAX's OIMTM software. The Vickers microhardness of different regions of the friction stir welded joint was measured on the ND–CWD plane at 3 mm from the root face (i.e. mid-thickness) using 100 g load for 15 s.

3. Results and discussion

3.1. Microstructural observation

The initial microstructures, grain sizes, and misorientation angle distributions of the AA2024–T351 and AA6061–T6 alloys before welding are shown in Figs. 2 and 3 respectively. The HAGBs identified by the angle of misorientation over 15◦are presented as bluelines, while low angle grain boundaries (LAGBs) are shown by green lines in the boundary misorientation maps (Figs. 2 and 3b). The average size of _-Al grains in the AA2024 and AA6061 are 49.8and 56.5 _m, respectively. As seen, the microstructures of the both sheets are characterized by coarse grains, a large number of HAGBs and lots of precipitates such as Mg2Si (for AA6061), CuAl2andCuAl2Mg (for AA2024) appear in the grain interior and at the grain boundaries. It should be noted that the blue blocks indicated by red arrows in the boundary misorientation map (Figs. 2 and 3c) are the precipitate particles. It

is clear that the size of precipitate particles in the AA6061 is much higher than the AA2024. The average mis-orientation angle of the AA2024–T351 and AA6061–T6 is 38.4◦and39.1◦, respectively. Orientation images and boundary maps are taken from transition zones between SZ and TMAZ in the advancing (AA2024) and the retreating (AA6061) sides are presented in Fig. 4 and the corresponding SEM images are shown in Fig. 5. Also, the grain size and misorientation distributions of the advancing and the retreating sides are also presented in Figs. 6 and 7 respectively. Moreover, the corresponding kernel average misorientation (KAM) maps are shown in Fig. 8.Fig. 4 reveals that the SZ of both sides has a fine equiaxed grain structure with a high fraction of HAGBs. These suggest the occurrence of dynamic recrystallization (DRX) phenomena due to the severe plastic deformation at high temperature during the friction stir welding. However, the static recrystallization (SRX) can take place after DRX during the cooling cycle. Results show that the grainsize on the retreating side is smaller than that on the advancing side. The grain sizes in the stirred zone on the advancing and retreating sides are 4.4 and 2.9 m, respectively. It can be concluded that the continuous grain growth (CGG) of dynamically recrystallized grains in the stirred zone on the advancing side is initiated. These grains are slightly coarsened after the plastic deformation because of static annealing during the weld cooling cycle.

Fig. 5 shows precipitate particles and voids in the microstructures of welded joint. It should be noted that many voids formed due to electropolishing treatment. During electropolishing, since galvanic corrosion accrues between the particles and matrix, the precipitates are separated from aluminium matrix and therefore, the voids create. Therefore, the voids can be considered as the particles in EBSD results. With regard to Figs. 4 and 5, the precipitate particles are not indexed and thus indicated by blue blocks. On the other hand, comparison between Figs. 4 and 5 demonstrates some blue blocks are not particles. For this reason, it is essential to consider the SEM images of samples in order to recognize the particles.

From Figs. 4(b) and (d), the fraction of precipitate particles in the SZ on the advancing side is much lower than that on the retreating side. At least two reasons may explain the obtained results:(1) The difference in temperature on advancing and retreating sides;(2) The difference in initial particle size (before FSW) of CuAl2andMg2Si precipitates. On the one hand, it is reported that the temperature of the materials on the advancing side is higher than that on the retreating side [1,6,14]. In the FSW, the material flow around the tool is moved from the advancing side to the retreating side additional to friction heat under the shoulder that gives higher temperature [1,6,14]. On the other hand, the initial particle size of the Mg2Si is higher than the CuAl2(see Figs. 2 and 3). Therefore, the rate of dissolution is greater on the advancing side than that on the retreating side dur-ing stir welding. Once the stirring pin has moved away from the stirred zone, the temperature decreases and therefore, the driving force for reprecipitation increases. However, decreasing the temperature leads to lower the atomic mobility and the equilibrium volume fraction of CuAl2particles is not reached in the stirred zone of the AA2024. It is well known that the precipitate particles pin the grain boundaries,

which hinder the boundary movement and the normal grain growth [15]. Thus, due to the small amount of precipitates in the SZ on the advancing side, a shortened period of time is necessary to enter the grain growth stage when compared to the retreating side. As also illustrated in Fig. 4, there are very coarse precipitate particles (higher than 10 _m in diameter) in the stirred zone of both sides of the weld joint. It should be noted that the rotation of tools promotes the dissolution of particles during stirring. At an appropriate rotation speed of pin (usually higher than 1000 rpm [16]), the precipitates can be fragmented and dissolved completely. However, in the present work, a tool rotation speed of 800 rpm is applied. For this reason, dissolution of the initial precipitates (demonstrated in Figs. 2 and 3) [16].It is interesting to note the stirred zone of AA2024 can be divided into two regions: (i) DRX + CGG region, and (ii) DRX region. Fig. 4(a)and (b) indicate that the grain size in the stirred zone adjacent tothe TMAZ (DRX region) is finer than the areas far away from TMAZ(DRX + CGG region). This can be explained since the materials in the DRX region are exposure to a lower temperature than materials in the SZ far away from thermomechanical affected zone. The lower temperature can decrease the migration velocity of grain boundaries and the grain growth rate. On the other hand, the lower temperature of the DRX region refine the CuAl2precipitate particles (see Fig. 4(b)) which can suppress the grain growth because of reducing the mobility of grain boundaries through Zener pinning mechanism. Fig. 4 shows a distinct boundary between the stirred zone and the TMAZ on the advancing side similar to the results reported in previous articles [1,7,17]. This is in contrast with the retreating side of the weld joint, where the boundary is more diffusive and rather unclear, thus the two zones are not easily distinguishable. This hap-pens because the strain rate and temperature gradients are much steeper on the advancing side than that on the retreating side. In fact, the AA6061 is exposed to the shear plastic deformation within a time shorter than the AA2024. This may be due to the torsion and the circumventing velocity fields having opposite directions in theAA6061, whereas these velocities have the same direction in theAA2024.Figs. 4(c) and (d) show lots of subgrains with low angle boundaries in the stirred zone on the retreating side which is formed by dynamic recovery (DRV) mechanism and also static recovery(SRV) after DRV during cooling cycle. It can be concluded that some regions of SZ do not undergo full dynamic recrystallization owing to the close proximity of these regions to the SZ/TMAZ transition zone

Since the stacking fault energy (SFE) of aluminium is high (approx. 166 mJ m−2), the DRV readily occurs. Therefore, for the occurrence of DRX, a critical condition (strain and temperature) is required which is not provided in the region adjacent to the TMAZ of AA6061.The TMAZ of both advancing and retreating sides has an elongated structure with the average grain size of 66.6 and 13.9 _m, respectively. The TMAZs have a deformed structure after under-going both plastic deformation and thermal cycle. However, the extent of plastic deformation and recrystallization in TMAZ are

Less than SZ. The microstructure of the TMAZs indicates that the original grains become heavily distorted as a result of material plastic flow during the stirring. In addition, there are a

large number of low angle grain boundaries due to the occurrence of DRV(see Fig. 7). Besides the DRV, continuous dynamic recrystallization(CDRX) is also taking place in the both TMAZs. The CDRX initiates by DRV and the development of HAGBs during CDRX is related to the repeated absorption of dislocations into subgrain boundaries and grain boundary sliding induced subgrain rotation. As can be seen in Figs. 4 and 7, the LAGBs fraction of TMAZ on the advancing side is higher than that on the retreating side. This is proved by corresponding kernel average misorientation maps as shown in Fig. 8. It can be said that, the extent of CDRX in the AA2024is lower than in the AA6061 and recrystallized grains are rarely seen on the advancing side. This is because of the very slow absorption rate of dislocations into subgrain boundaries on the advancing side. There are two reasons for this:(1) The volume fraction of fine precipitate particles: The volume content of fine particles in the TMAZ of the AA2024 is much higher than the AA6061 (see Fig. 4(b) and (d)). The fine precipitate particles (less than 1 _m in diameter) make the motion of dislocations difficult as they may pin lattice dislocations, thereby, hindering further movement. Since the temperature in TMAZ is not as much as that in SZ, the driving force necessary for non-conservative dislocation motion (i.e. climb) onto an adjacent slip plane and bypass the fine precipitate particles is not provided in the AA2024.(2) SFE: The stacking fault energy also has a strong influence on the dislocations movement. In order to reduce the stored energy in the crystal, the perfect dislocations will dissociate into a pair of Shockley partial dislocations. The separation of partial dislocations in a low SFE material is higher than that in the high SFE one. Therefore, the cross-slip of screw dislocations is difficult in the materials with low stacking fault energy, since the occurrence of the cross-slip can only be achieved by recombination of the two Shock-ley partials to a perfect dislocation. Consequently, the dislocation movement is restricted to the original slip plane. As mentioned before, the aluminium alloys have high SFE, however, the SFE ofAA2024 is lower than that of AA6061 [18] and thus the dislocation motion through cross-slip is difficult in TMAZ on the advancing side.

3.2. Texture evolution

Fig. 9 illustrates the {100}, {110}, and {111} pole figures of the initial AA2024 and AA6061 sheets. Also, the orientation distribution functions of the starting materials are shown in Fig. 10. One should note that the intensities of texture components expressed in multiple of the random density (×R) unit. Then on-symmetrized PFs indicate a relatively full symmetry i.e. symmetric positions of orientations in the initial sheets. As seen, the main texture components of the AA2024 are {011}_011_ Rotated Goss, {001}_100_ Cube, {001}_100_ Rotated Cube, {112}_241_, {44 11}_11 11 8_ Dillamore, {112}_111_ Copper, {123}_634_ S, and{011}_115_ Goss/Brass with the peak intensity of 12.1 × R, 11.8 × R,4.9 × R, 4.2 × R, 2.6 × R, 2.3 × R, 2.2 × R, and 1.9 × R, respectively. On the other hand, the major orientations of the AA6061 can be char-acterized as {001}_100_ Cube, {011}_011_ Rotated Goss, {112}_011_Rotated Copper, and {011}_211_ Brass with the maximum intensity of 5.2 × R, 2.4 × R, 1.8 × R, and 1.5 × R, respectively. In both samples, Cube and Rotated Goss texture

components are quite strong. There is no evidence of _-fibre, _-fiber, _-fiber, and _-fibre in both alloys.

Fig. 11 shows the {100}, {110}, and {111} PFs of the advancing and the retreating sides. Also, the ODFs on both sides are presented in Fig. 12. The pole figures indicate that the crystallo-graphic textures are asymmetric for advancing and retreating sides. The PFs are asymmetric as a result of heterogeneous plastic flow during FSW. The texture components obtained after FSW on the advancing side can be characterized as the {011}_211_, {221}_012_,{123}_634_, {001}_110_, {112}_011_, {223}_112_, and {001}_100_with the maximum intensity of 7.3 × R, 6.8 × R, 3.5 × R, 2.7 × R,2.3 × R, 2.1 × R, and 1.4 × R, respectively. Also, the {031}_213_,{111}_112_, {001}_110_, {112}_111_, {123}_634_, and {111}_110_orientations developed in the retreating side with the peak texture intensity of 9.4 × R, 6.7 × R, 2.8 × R, 2.6 × R, 2.2 × R, and 2.1 × Respectively. Moreover, Fig. 12(b) clearly shows that the fibre

(_111_//ND) texture evolved in the retreating side which is effective for improving the formability of the FCC metals and alloys. The results indicate that after FSW, the textures on both sides are completely different as compared to initial samples. In the advancing side, the overall texture strength is weaker than the initial AA2024 sheet. By comparing the ODF in Fig. 10 (a)with that in Fig. 12(a), it can be found that the intensity of {001}_100_, {001}_110_, and {112}_241_ orientations decreased and the {123}_634_ component weakened. Also, some textures such as {011}_011_, {4 4 11}_11 11 8_, and {112}_111_ Copper disappeared, while new components including strong {011}_211_ and{221}_012_ orientations and moderate {112}_011_ and {223}_112_created. Development of the intense {011}_211_ texture during friction stir welding is considered to be due to the rotations of both {011}_011_ and {001}_100_ orientations. The {011}_011_and {001}_100_ components rotate into {011}_211_ texture dur-M.M. Moradi et al. / Journal of Manufacturing Processes 32 (2018) 1–10 9 Fig. 12. Orientation distribution functions of (a) advancing and (b) retreating sides. Fig. 13. Microhardness profile across the weld region in FSW mainly through the activity of {111}_110_ slip system. The{011}_011_ transforms to {011}_211_ via 55◦lattice rotation about normal direction i.e. _011_. Also, the grains with {001}_100_ texture rotates toward {011}_211_ through 45◦rotation around rolling direction i.e. _100_, followed by 35◦rotation about ND. Interestingly, an uncommon shear component namely {221}_012_ generated owing to shear deformation during friction stirring. This orientation is close to {111}_112_ and {111}_110_ which are conventional shear components.It should be noted that a weak recrystallization component namely {001}_100_ also existed on the advancing side. This can be due to discontinuous static recrystallization (DSRX) and/or meta-dynamic recrystallization (MDRX) mechanisms. In general, the initial {001}_100_ texture will be removed after plastic deformation and the grains with {001}_100_ orientation rotate toward other components. Thus, the {001}_100_ component in advancing side(Fig. 12(a)) produced during and/or after stirring and is not related to initial texture of sheet. Among various recrystallization mechanisms, only DSRX and MDRX can

be responsible for this result. The DSRX is associated with the nucleation of new grains and with their growth during the weld cooling cycle. Also, the MDRX phenomenon involves dynamic nucleation (during stirring) and static growth (after stirring) of recrystallized grains. Therefore, both mechanisms can create the new grains with the {001}_100_ orientation without any subsequent rotations.The textures evolution in the retreating side of welded joint is different from that on the advancing side. Unlike the advancing side, the overall texture strength of retreating side is stronger than the initial AA6061 sheet. By comparing the ODF in Fig. 10(b)with that in Fig. 12(b), it can be seen that initial {001}_100_,10 M.M. Moradi et al. / Journal of Manufacturing Processes 32 (2018) 1–10 {011}_011_, {112}_011_, and {011}_211_ orientations completely eliminated on the retreating side. Also, some textures including intense {031}_213_ and {111}_112_ components, and moderate{001}_110_, {111}_110_ created suggesting a complicated plastic flow during friction stirring. The results indicated that more than one shear texture is active on the advancing side of the weld. The formation of shear textures such as {031}_213_, {111}_112_,{001}_110_, {111}_110_ components during FSW is due to the severe shear strain produced on the retreating side. This is consistent with the literature [4,10,11]. Some main shear components including {111}_110_ and {111}_112_ are described by a _-fibre texture, which runs from the (111)[1¯10] orientation through the(111)[1¯21] component to the (111)[0¯11] component, and finally to the (111)[¯1¯12] orientation, as seen in Fig. 10(b). In these cases, the(111) plane is oriented towards the ND and the _110_ or _112_ inside the (111) plane are along the Wit is noticed that, unlike the advancing side, there is no sign of {001}_100_ recrystallization component on the retreating side. However, Fig. 4(c) and (d) clearly indicated the occurrence of recrystallization. At least two reasons may explain this result: (1) Occurrence of CDRX which leads to different final orientations for recrystallized grains through various rotations of subgrain; and/or(2) Partially rotation of DDRX grains during the final stage of deformation.

3.3. Microhardness

The microhardness profile of the dissimilar friction stir welded joint is illustrated in Fig. 13. It should be noted that the microhard-ness profile on the advancing side is almost identical (118–140 HV),while the microhardness profile reveals three distinguishable regions on the retreating side: the softest corresponds to SZ and TMAZ (62–70 HV); the hardest matches the BM (103–105 HV); and the HAZ exhibits the microhardness values amongst the other two regions (75–98 HV). On the retreating side, the microhardness of the SZ and TMAZ exhibited a significant decrease compared to that of the BM; because the hardness of AA6061 alloy mainly depends on the size and amount of precipitate particles. As seen in Fig. 5(b), most particles were dissolved in the TMAZ and the precipitates coarsened or partially dissolved in the stirred zone. As previously described in Section 3.1, the average grain size of the TMAZ on the advancing side was much higher than that of the stirred zone, while the microhardness in the SZ shows only a modest increase com-pared to that of the TMAZ on the

advancing side. This is mainly due to the presence of many precipitates particles in the TMAZ (see Fig. 5(a)).

4. Conclusions

In the present study, AA2024 and AA6061 alloys were friction stir welded. The microstructure and crystallographic texture evolution were examined and compared in detail. Based on the experimental results, the following main conclusions can be made:

1 The stirred zone on both advancing and retreating sides had affine equiaxed grain structure with a large fraction of high angle boundaries owing to the occurrence of both dynamic and static recrystallizations.

2 The volume fraction of precipitates in the stirred zone on the retreating side was much higher than that on the advancing side because of the difference in (1) temperature on the advancing and retreating sides, and (2) initial size of precipitates.

3 The extent of continuous dynamic recrystallization (CDRX) in the TMAZ on the advancing side was smaller than that on the retreating side as a result of the slow absorption rate of dislocations into subgrain boundaries on the advancing side.

4 The overall texture intensity was decreased on the advancing side but was increased on the retreating side as compared to the initial sheets. The initial components could be completely removed on both sides and some strong shear textures could be formed due to the severe shear deformation during FSW.

5 The {001}_100_ recrystallization component was generated on the advancing side due to discontinuous static recrystallization (DSRX) and/or meta-dynamic recrystallization mechanisms(MDRX).

References

[1] Kumar N, Yuan W, Mishra RS. Friction stir welding of dissimilar alloys and materials. first edition Oxford, United Kingdom: Elsevier Science Ltd.; 2015.

[2] Jamshidi Aval H. Microstructure and residual stress distributions in friction stir welding of dissimilar aluminium alloys. Mater Des 2015;87:405–13.

[3] Aydin H, Bayram A, Uguz A, Akay KS. Tensile properties of friction stir welded joints of 2024 aluminium alloys in different heat-treated-state. Mater Des2009;30:2211–21.

[4] Wang B, Lei B, Zhu J, Feng Q, Wang L, Wu D. EBSD study on microstructure and texture of friction stir welded AA5052-O and AA6061-T6 dissimilar joint. Mater Des 2015;87:593–9.

[5] Guo JF, Gougeon P, Chen XG. Characterisation of welded joints produced by FSW in AA1100–B4C metal matrix composites. Sci Technol Weld Join2012;17:85–91.

[6] Salih OS, Ou H, Sun W, McCartney DG. A review of friction stir welding of aluminium matrix composites. Mater Des 2015;86:61–71.

[7] Venkateswarlu D, Nageswararao P, Mahapatra MM, Harsha SP, Mandal NR.Processing and optimization of dissimilar friction stir welding of AA2219 andAA7039 alloys. J Mater Eng Perform 2015;24:4809–24.

[8] Hu ZL, Wang XS, Yuan SJ. Quantitative investigation of the tensile plastic deformation characteristic and microstructure for friction stir welded 2024aluminium alloy. Mater Charact 2012;73:114–23.

[9] Guo J, Gougeon P, Chen XG. Microstructure evolution and mechanical prop-erties of dissimilar friction stir welded joints between AA1100-B4C MMC andAA6063 alloy. Mater Sci Eng A 2012;553:149–56.

[10] Xu X, Lu Y, Zheng F, Chen B. Microstructural investigation of friction-stir-welded 7005 aluminium alloy. J Mater Eng Perform 2015;24:4297–306.

[11] Imam M, Racherla V, Biswas K, Fujii H, Chintapenta V, Sun Y, et al. Microstructure-property relation and evolution in friction stir welding of naturally aged 6063 aluminium alloy. Int J Adv Manuf Technol 2017;91:1753–69.

[12] Peel M, Steuwer A, Preuss M, Withers PJ. Microstructure, mechanical properties and residual stresses as a function of welding speed in aluminium AA5083friction stir welds. Acta Materialia 2003;51:4791–801.

[13] Prangnell PB, Heason CP. Grain structure formation during friction stir welding observed by the ‘stop action technique. Acta Materialia 2005;53:3179–92.

[14] Lohwasser D, Chen Z. Friction stir welding from basics to applications. first edition Cambridge, United Kingdom: Woodhead Publishing Limited; 2010.

[15] Humphreys FJ, Hatherly M. Recrystallization and related annealing phenom-ena. second edition Oxford, United Kingdom: Elsevier Science Ltd.; 2004.

[16] Mao Y, Ke L, Liu F, Huang C, Chen Y, Liu Q. Effect of welding parameters on microstructure and mechanical properties of friction stir welded joints of 2060aluminium lithium alloy. Int J Adv Manuf Technol 2015;81:1419–31.

[17] Threadgill PL, Leonard AJ, Shercliff HR, Withers PJ. Friction stir welding of aluminium alloys. Int Mater Rev 2009;54:49–93.

[18] Muzyk M, Pakiela Z, Kurzydlowski KJ. Ab initio calculations of the generalized stacking fault energy in aluminium alloys. Scripta Materialia 2011;64:916–8.

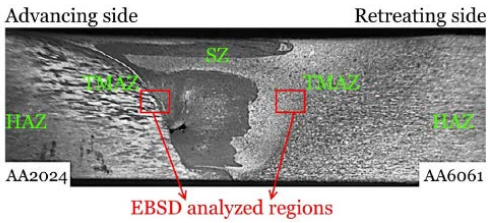

Fig. 1. Macroscopic photograph of the dissimilar friction stir welded joint.

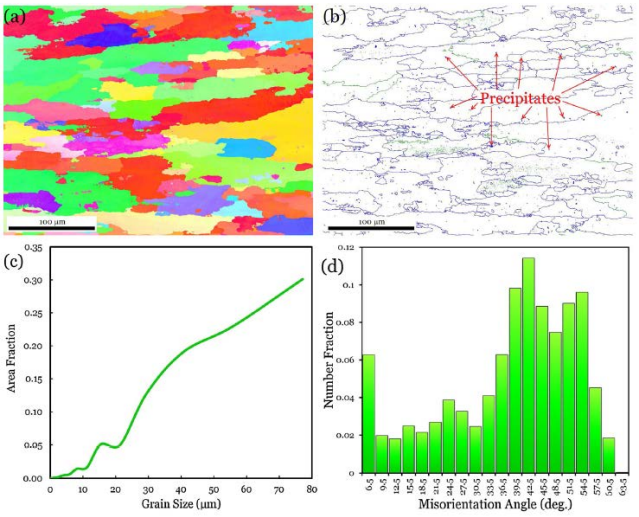

Fig. 2. (a) Grain orientation map, (b) grain boundary map, (c) grain size distribution, and (d) misorientation angle distribution of the initial AA2024 sheet.

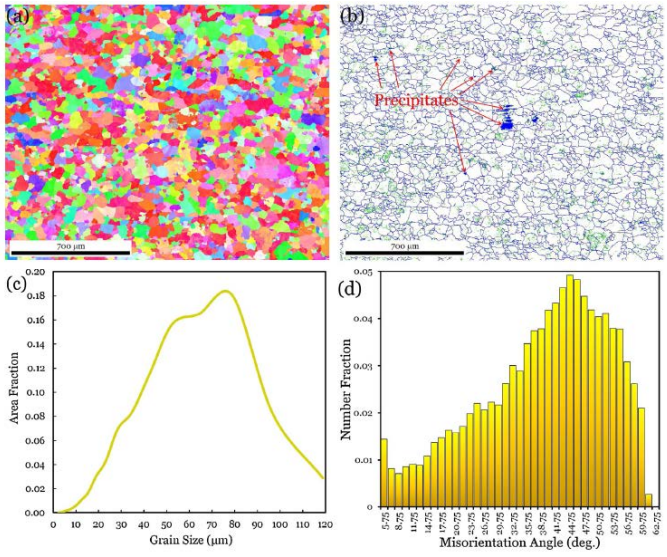

Fig. 3. (a) Grain orientation map, (b) grain boundary map, (c) grain size distribution, and (d) misorientation angle distribution of the initial AA6061 sheet.

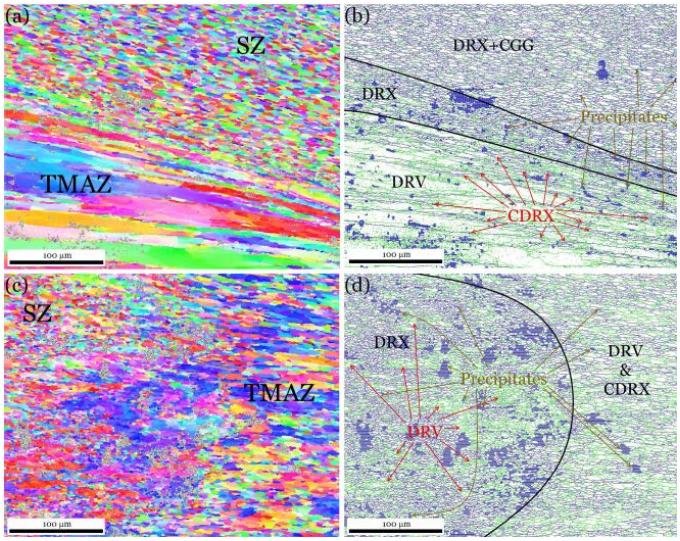

Fig. 4. Orientation imaging and grain boundary maps of transition zones between SZ and TMAZ in the (a,b) advancing side and (c,d) retreating side.

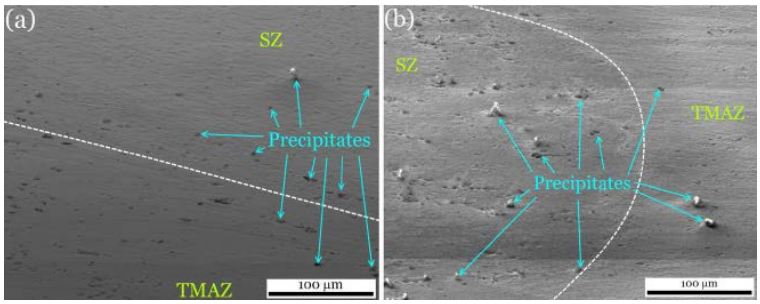

Fig. 5. SEM images of transition zones between SZ and TMAZ in the (a) advancing side and (b) retreating side. And thus insufficient strain and/or temperature.

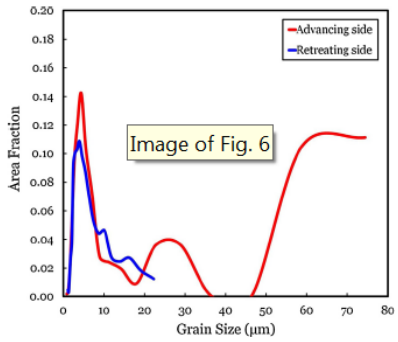

Fig. 6. The grain size distribution of advancing and retreating sides.

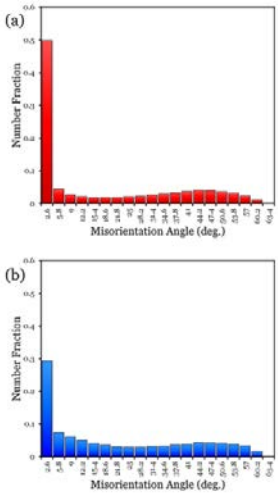

Fig. 7. The misorientation angle distribution of (a) advancing and (b) retreating sides.

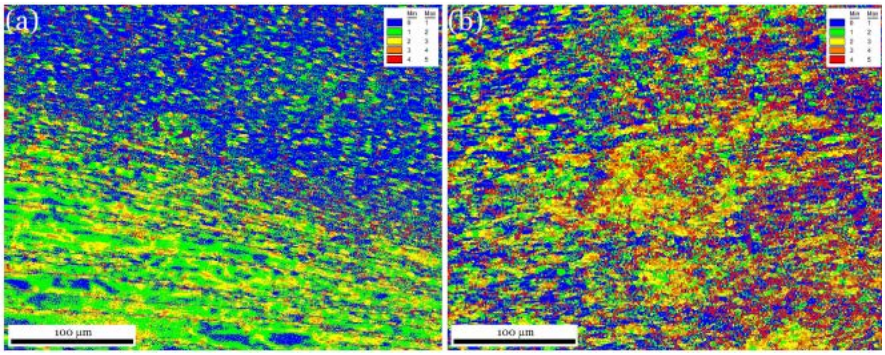

Fig. 8. KAM maps of transition zones between SZ and TMAZ in the (a) advancing side and (b) retreating side.

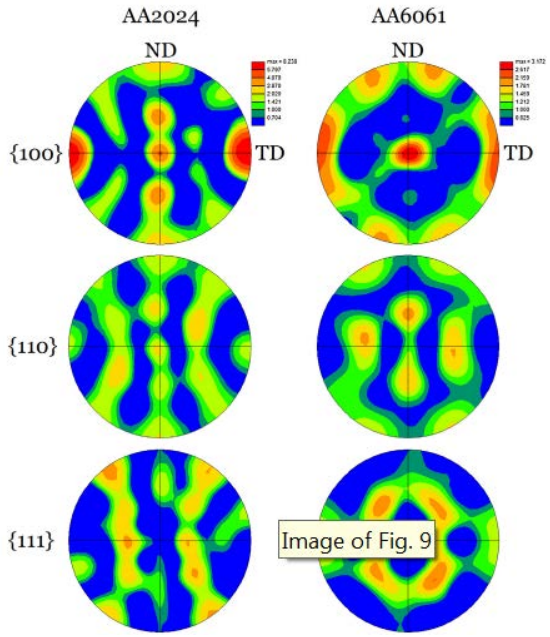

Fig. 9. {100}, {110}, and {111} pole figures of initial AA2024 and AA6061 sheets.

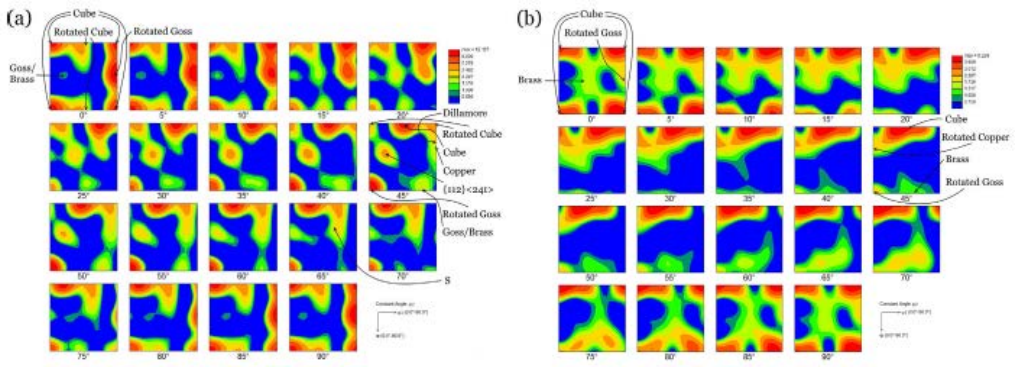

Fig. 10. Orientation distribution functions of initial (a) AA2024 and (b) AA6061 sheets.

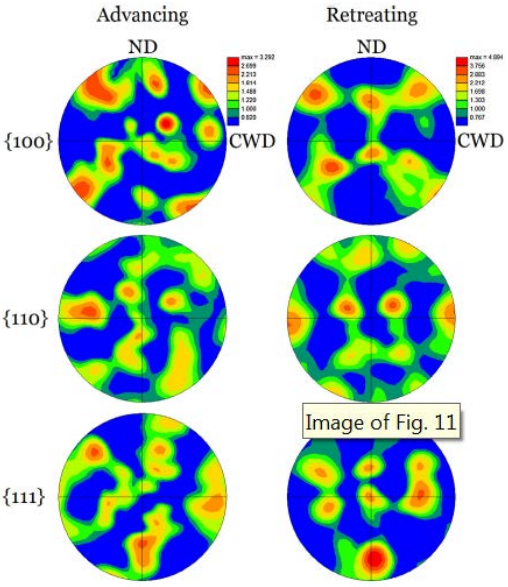

Fig. 11. {100}, {110}, and {111} pole figures of advancing and retreating sides.

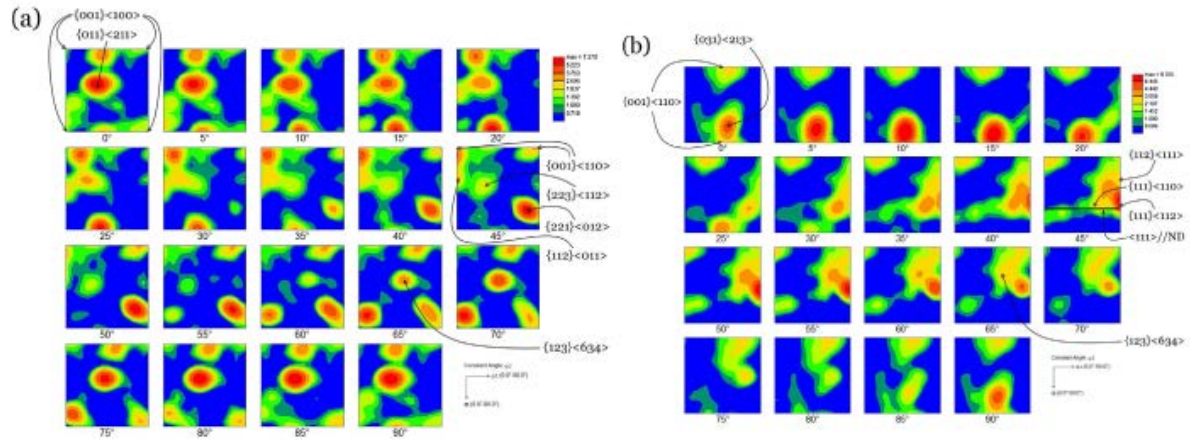

Fig. 12. Orientation distribution functions of (a) advancing and (b) retreating sides.

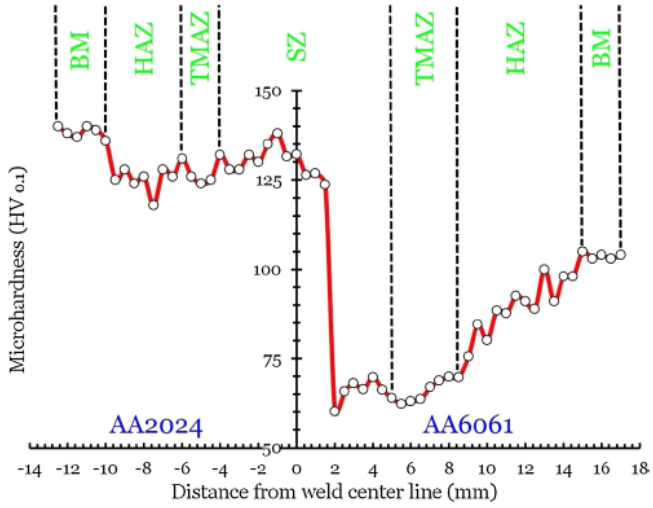

Fig. 13. Microhardness profile across the weld region